Journal of Advanced Ceramics
2024, **13**(11): 1748–1758
https://doi.org/10.26599/JAC.2024.9220971

Research Article

Breaking the trade-off of hardness–ductility in $(Cr_{1-x}Mo_x)_2AlC$ MAX phase coatings via a hierarchical structure

Yan Zhang[1], Shuowen Zhang[3], Anfeng Zhang[1], Guanshui Ma[1], Kaihang Wang[1], Zhenyu Wang[1], Aiying Wang[1,2]✉

[1] *Key Laboratory of Advanced Marine Materials, Ningbo Institute of Materials Technology and Engineering, Chinese Academy of Sciences, Ningbo 315201, China*
[2] *Center of Materials Science and Optoelectronics Engineering, University of Chinese Academy of Sciences, Beijing 100049, China*
[3] *Ningbo Institute of Materials Technology and Engineering, Chinese Academy of Sciences, Ningbo 315201, China*

Received: July 9, 2024; Revised: August 22, 2024; Accepted: September 15, 2024

Abstract: The Cr_2AlC MAX phase offers a remarkable combination of excellent electrical conductivity and hot corrosion resistance in extremely harsh environments. However, the strong trade-off between hardness and toughness is rather limited by its nanolaminate structure for desired applications. Taking the solid solution strengthening and gradient hardening synergy, in this work, high-purity Cr_2AlC coatings with various Mo solid solutions were successfully fabricated via a hybrid sputtering technique followed by subsequent annealing. Interestingly, gradually changing the Mo concentration in the $(Cr_{1-x}Mo_x)_2AlC$ (x = 0.05–0.24) coating enabled a hierarchical structure responsible for gradient refinement of the crystal grain size, and the solid solution of Mo atoms at Cr sites and the gradient variation in the Mo content were confirmed via the atomic-resolution transmission electron microscopy (TEM) characterization. Compared with those of the pristine Cr_2AlC coating, the nanoindentation hardness and toughness values of H/E and H^3/E^2 for the hierarchical $(Cr_{1-x}Mo_x)_2AlC$ coating were enhanced by approximately 26%, 12%, and 57%, respectively. On the basis of comprehensive experiments and *ab initio* simulations, the reasons behind this observation were mainly attributed to the synergistic effect of Mo occupancy with strong bonding at the Cr site and the strengthening of grain refinement induced by the gradient Mo concentration in the $(Cr_{1-x}Mo_x)_2AlC$ coating. These findings not only reveal the underlying mechanism for the Mo solid solution in the Cr_2AlC coating but also offer a new concept for developing ultrahigh-strength ductility materials for the laminar MAX phase.

Keywords: MAX phase coating; Mo solid solution; hierarchical structure; density functional theory (DFT); hardness–ductility

1 Introduction

$M_{n+1}AX_n$ phases, also empirically known as MAX phases, are a group of ternary carbide or nitride ceramics inherently composed of a hexagonal layered structure. Here, M represents a transition metal element; A signifies an element from the group A; X stands for either carbon or nitrogen. In most cases, n typically ranges from 1 to 4, corresponding to the abbreviations of 211, 312, and 413 phases. Various MAX phase ceramics featuring B as the X element have also been investigated for their desired properties [1–6]. In general, $M_{n+1}X_n$ layers are interleaved with A layers along the c-axis, in which the $M_{n+1}X_n$ layers are composed of edge-shared M_6X octahedra with robust M–X bonds, whereas relatively weak M–A bonds dominate the connections between the $M_{n+1}X_n$ layers and the A layers. This unique combination of covalent-ionic-metallic bonds in MAX phases endows them with remarkable properties stemming from both ceramics and metals, such as easy machinability, good electrical conductivity, excellent anti-corrosion and oxidation resistance, and outstanding ability to withstand thermal shock [7,8]. Compared with bulk MAX phases, MAX phase coatings are considered among the strongest candidates for protective components when subjected to ultrahigh-temperature and/or harsh corrosive irradiation environments [9–11].

✉ Corresponding author.
E-mail: aywang@nimte.ac.cn

As a most important example of MAX phases, Cr_2AlC coatings have gained increasing attention because of the presence of M-position Cr and A-position Al, where both Cr and Al easily form a dense oxide layer on the surface for protection and self-healing [12–14]. However, the relatively low hardness, which is generally less than 15 GPa for Cr_2AlC MAX phase coatings, strongly limits its wide application [15]. Inspired by the contribution of $M_{n+1}X_n$ bonds to mechanical properties, the introduction of a solid solution at the M-site has been confirmed to increase the hardness of MAX phases. For example, Qu *et al.* [16] fabricated bulk $(Ti_{1-x}Zr_x)_3SiC_2$ MAX phases at 1450–1750 °C via spark plasma sintering (SPS), in which the hardness was improved to 16.3±1.1 GPa, in contrast to the 12.7±1 GPa for pristine Ti_3SiC_2. Furthermore, compared with the original Cr_2AlC coating, the substitution of Cr with some V in the Cr_2AlC matrix led to a 34.3% increase in hardness and a 23.6% increase in elastic modulus, which was accompanied by a 25% decrease in the friction coefficient due to the formation of lubricated phases such as V_2O_5 [17]. Nevertheless, the opening challenge is still faced with how to fabricate high-purity MAX phase coatings with M-site solution treatment but without intermetallic impurities and how to overcome the trade-off between strength and ductility without deteriorating other superior properties.

If one considers the unique atomic bonds in the MAX structure, the replacement of M-site Cr by the neighboring atom of Mo in the same group will be an alternative solution. Clearly,

Mo has been frequently employed as a reinforcing phase in oxide or carbide coatings because of its high hardness and strong corrosion resistance [18–20]. Additionally, manipulation of gradient grain structures also represents a strategy for overcoming the strength–toughness trade-off in metallic materials [21]. Very recently, our work demonstrated that the fabricated $(Cr_{0.9}Mo_{0.1})_2AlC$ solid solution coating significantly increased the corrosion current density and electric impedance by almost 10 times in a 3.5 wt% NaCl solution [22]. The reason could be the accelerated passivation layer rich in aluminum oxides by the Mo solid solution on the coating surface. However, the effect of a Mo solid solution on the mechanical properties of the Cr_2AlC MAX phase has yet to be studied. Therefore, in this work, we fabricated $(Cr_{1-x}Mo_x)_2AlC$ MAX coatings with various Mo concentrations (x = 0.05–0.24) via a multitarget magnetron sputtering technique combined with *ex situ* vacuum annealing. Most importantly, synergistic concepts evolved by introducing a Mo solid solution to the Cr_2AlC matrix and manipulating the hierarchical structure while refining the grain size to achieve hardness-toughness strengthening simultaneously. The chemical composition and structural characteristics of $(Cr_{1-x}Mo_x)_2AlC$ MAX coatings were comprehensively investigated via atom-resolved transmission electron microscopy (TEM) and *ab initio* simulations. The underlying mechanisms for the evolution of mechanical properties were discussed in terms of microstructural evolution with various Mo occupancies at Cr sites, as well as the parallel existence of hierarchical structures with gradient changes in crystal grain sizes.

2 Methodology

2.1 Coating deposition

$(Cr_{1-x}Mo_x)_2AlC$ (x = 0.05–0.24) coatings were deposited on Ti–6Al–4V substrates via a custom-made magnetron sputtering deposition system with multiple targets, followed by *ex situ* vacuum annealing. Figure 1 shows a schematic diagram of the hybrid procedure for coating. A rectangular $Cr_{1.5}Al$ compound target (purity: 99.99 wt%) and a rectangular molybdenum target (purity: 99.99 wt%) of the same size (400 mm × 100 mm × 7 mm) were used as cosputtering sources for Cr, Al, and Mo deposition. Specifically, a high pulsed impulse power (HiPIMS) supply, which has a high ionization rate and plasma density, was introduced to the $Cr_{1.5}Al$ target with a current of 3 A, whereas a DC power supply was applied to the molybdenum target. The Ar/CH^4 precursor was used to generate Ar^+ and carbon ions. Prior to deposition, the polished substrates were ultrasonically cleaned with acetone and alcohol for 15 min each and then put into the deposition chamber. These samples were fixed on a rotational substrate holder in front of a $Cr_{1.5}Al$ target at a distance of approximately 12 cm, thereby initiating the Ar^+ etching process powered by a linear ion beam source and substantial coating deposition. The deposition process of the coating lasted for 3 h at a temperature of 150 °C, and the sputtering current of the Mo target was changed every hour. Notably, the Mo concentration in the $(Cr_{1-x}Mo_x)_2AlC$ coatings was controlled by meticulously fine-tuning the sputtering current of the Mo target at 0.4, 0.7, and 1.0 A, respectively. Thus, the sputtering time for each layer of the $(Cr_{1-x}Mo_x)_2AlC$ hierarchical coating is 1 h. After deposition, the as-deposited coatings were transferred to a thermal furnace for annealing at 550 °C for 5 h to obtain $(Cr_{1-x}Mo_x)_2AlC$ phases, during which the vacuum pressure was maintained at 3.0×10^{-4} Pa. The heating rate and cooling rate during thermal treatment were 10 and 5 °C/min, respectively. For comparison, a Cr_2AlC coating was also fabricated via the same procedure but without an operating Mo sputtering target.

2.2 Characterization methods

The phase composition of the $(Cr_{1-x}Mo_x)_2AlC$ coatings was analyzed via an X-ray diffractometer (XRD; Bruker D8 Advance, Germany), where the data were collected via a step-scanning diffractometer with Cu Kα radiation (λ = 0.154 nm). The surface/cross-sectional morphology and chemical composition of the coatings were characterized by a scanning electron microscope (SEM; Verios G4 UC, USA) with an energy-dispersive X-ray spectrometer (EDS) and a transmission electron microscope (TEM; Spectra 300, USA). The samples for TEM testing were specifically cut and thinned via the focused ion beam (FIB) technique (Thermo Scientific Helios-G4-CX, USA).

The mechanical properties of the coatings were measured via a nano indenter (MTS-G 200, KLA Co., USA) with a Berkovich diamond tip in continuous stiffness measurement (CSM) mode. The maximum indentation depth was selected to be 1000 nm, and the average values of hardness and elastic modulus were chosen at the stabilized loading region of 500–600 nm (nearly less than 1/10 thickness of the coating) to diminish the influence of the substrate. Furthermore, the fracture toughness of the coatings was assessed through nanoindentation experiments with a sharp cube-corner tip, identifying the cracks adjacent to the indentation region. During this procedure, a specific load of 25 mN was applied to the samples.

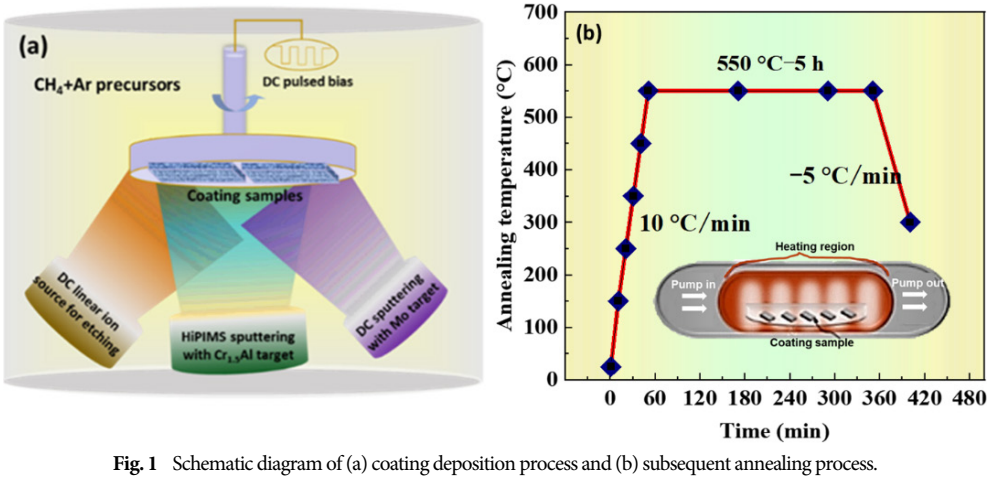

Fig. 1 Schematic diagram of (a) coating deposition process and (b) subsequent annealing process.

清華大学出版社 Tsinghua University Press | SciOpen

2.3 Computational details

Structural optimization of the $(Cr_{1-x}Mo_x)_2AlC$ compounds with $P6_3/mmc$ symmetry was performed via the CAmbridge sequential total energy package (CASTEP) [23,24], which uses density functional theory (DFT) based on the plane-wave pseudopotential method. The generalized gradient approximation constructed by Perdew–Burke–Ernzerhof (GGA-PBE) [25] was specifically adopted for the exchange-correlation energy functional. In this work, a 2 × 2 × 1 supercell with 32 atoms was constructed. A 10 × 10 × 2 Monkhorst–Pack *k*-point grid and 480 eV cutoff energy were used in the calculations of the elastic constants, charge distribution, and partial density of states [26]. Convergence tests revealed that with these parameters, the relative energy converged to better than 10^{-5} eV/atom, with 0.01 eV/Å as the maximum force per atom. The elastic properties were calculated through the utilization of the finite strain methodology integrated within the CASTEP code [27]. This technique allows the application of a set of finite uniform deformations and yields the resulting stresses subsequent to the optimization of the internal degrees of freedom. A maximum amplitude of 0.003 Å was selected for each of the six step strains. Pugh's ratio *B*/*G* (the ratio of the bulk modulus to the shear modulus) was used to determine the brittleness or ductility of the $(Cr_{1-x}Mo_x)_2AlC$ compounds.

3 Results and discussion

3.1 Microstructural analysis of $(Cr_{1-x}Mo_x)_2AlC$ coating

Figure 2(a) shows the XRD diffractograms of the pristine Cr_2AlC coating and the solid-treated $(Cr_{1-x}Mo_x)_2AlC$ coating for comparison. In addition to the obvious peak at 71°, which originated from the Ti–6Al–4V substrate, the two coatings presented dominant peaks at 2θ approximately 37° and 42°, which could be assigned to the (101) plane and (103) plane of the Cr_2AlC coating. Moreover, the other peaks at 14° and 77° were correlated to the (002) plane and (109) plane of the Cr_2AlC crystal structure (PDF#00-029-0017). Notably, the introduction of a Mo solid solution in the Cr_2AlC coating led to the diffraction peak shifting downward compared with that in the case without Mo. Figure 2(b) shows the distinct changes in the local magnified image at 2θ of approximately 42°, in which the peak was reduced from 42.1° to 41.9°. The reason was probably due to the relatively larger atomic radius of Mo (1.36 Å) than that of Cr (1.25 Å), which caused an increase in the lattice constant and a decrease in the peak. Weak peaks assigned to Cr_5Al_8 compounds indicated the formation of small amounts of impurities in both the Cr_2AlC and $(Cr_{1-x}Mo_x)_2AlC$ MAX phase coatings from the XRD diffractograms. However, owing to its relatively low intensity, Cr_5Al_8 could make rather minor or even negligible contributions to the evaluated mechanical properties, as predicted. Figure 2(c) further displays the surface morphology of the synthesized $(Cr_{1-x}Mo_x)_2AlC$ coating, where a homogeneous and dense structure without any visible cracks was clearly visible. These observations confirmed the successful manipulation of the high-purity $(Cr_{1-x}Mo_x)_2AlC$ MAX phase coating and the comparative Cr_2AlC coating.

Figure 3 shows the cross-sectional morphologies of the $(Cr_{1-x}Mo_x)_2AlC$ coatings and the corresponding EDS data from SEM analysis. There was an increasing trend in the Mo concentration along the growth direction of the coating. From the inside layer subjected to the substrate toward the outer surface layer, the Mo concentration was 2.2, 6.1, and 10.6 at%, respectively (Fig. 3(a)). Moreover, all the elements demonstrated a uniform distribution in each separative layer (Fig. 3(b)), indicating the facile advantages of current synthesis for M-site solid solutions in the MAX phase. As shown in Fig. 3(c), the detailed cross-sectional morphology of the $(Cr_{1-x}Mo_x)_2AlC$ coating also revealed that the gradual increase in the Mo concentration resulted in a remarkably hierarchical structure with refined crystal grains during coating growth, and the thickness of the coating was approximately 4 mm. In addition, such a coating possessed a strong adhesion strength without any spallation or delamination within the multilayer interfaces and the TC4 substrate.

To further analyze the changes in the concentration of Mo, an electron probe X-ray microanalyzer (EPMA) testing was employed, and the results are presented in Fig. 4. The Mo content clearly increases with the growth direction of the coating, and the proportions of Mo atoms in each layer are 2.64%, 7.14%, and 12.16%, which is essentially consistent with the EDS data (Fig. 3). In other words, the corresponding material compositions for each layer from the inner layer to the outer layer are $(Cr_{0.94}Mo_{0.05})_2AlC$, $(Cr_{0.86}Mo_{0.14})_2AlC$, and $(Cr_{0.76}Mo_{0.24})_2AlC$.

To gain insight into the microstructural evolution of the Mo solid solution in the hierarchical $(Cr_{1-x}Mo_x)_2AlC$ MAX coating, the atomic-resolution TEM characterization was further conducted. Figure 5(a) shows a low-resolution bright-field image of the cross-sectional feature and the selected area electron diffraction (SAED) pattern. The observation of a dense gradient structure in each layer was well aligned with the findings from the SEM results, indicating the predominant polycrystalline structure of the MAX phases. Moreover, the high-angle annular dark field (HAADF) image (Fig. 5(b)) revealed a discernible reduction in the grain size along the growth direction of the coating. The corresponding mapping EDS results validated the uniform distribution of each element (Cr, Mo, Al, and C) in each separative layer, which was consistent with the aforementioned

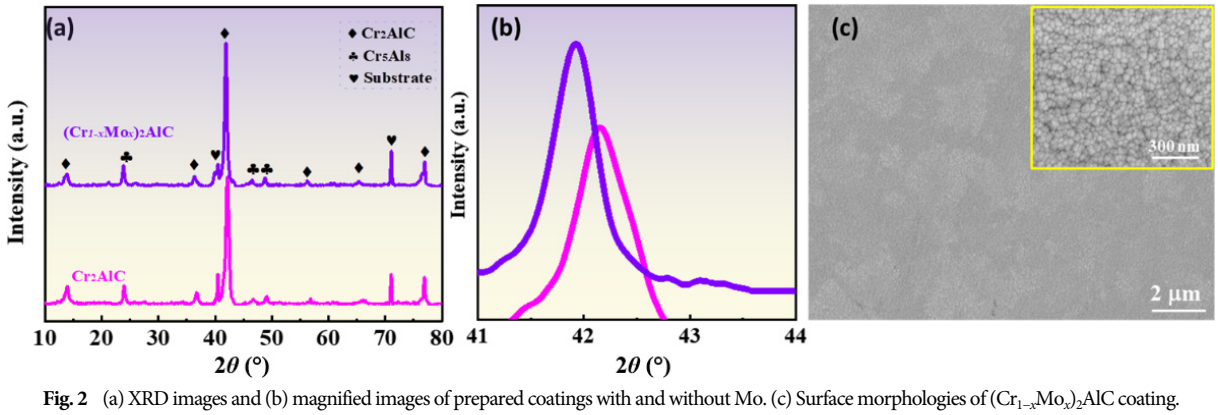

Fig. 2 (a) XRD images and (b) magnified images of prepared coatings with and without Mo. (c) Surface morphologies of $(Cr_{1-x}Mo_x)_2AlC$ coating.

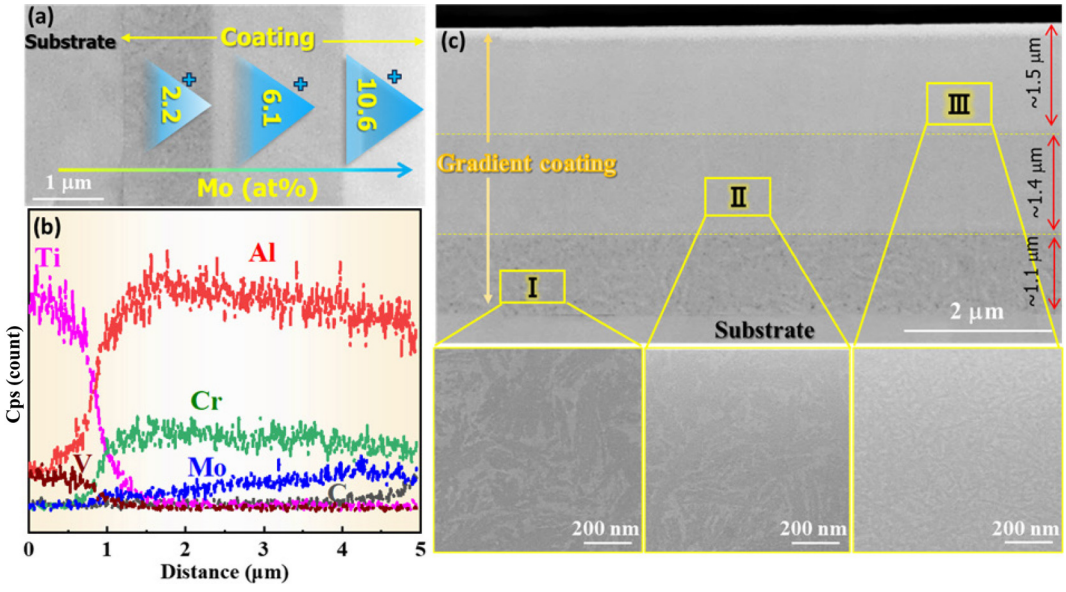

Fig. 3 (a) Cross-sectional morphology and (b) corresponding EDS results of $(Cr_{1-x}Mo_x)_2AlC$ coating. (c) SEM images with extensive morphology changes in each layer.

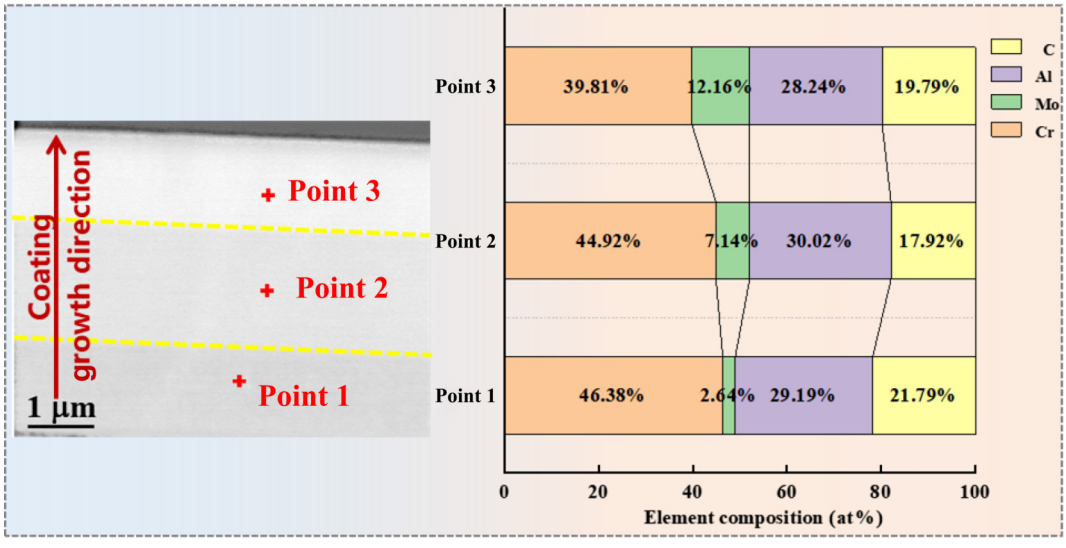

Fig. 4 EPMA results of $(Cr_{1-x}Mo_x)_2AlC$ coating.

analysis in Fig. 3. On the basis of the dark-field TEM image (Fig. 5(c)), the statistical distributions of the grain sizes during coating growth were approximately 70.04, 56.86, and 37.07 nm in each layer. This observation clearly revealed that increasing the Mo concentration in the $(Cr_{1-x}Mo_x)_2AlC$ coating led to gradient refinement of the crystal grain size toward an interesting hierarchical structure. Additionally, the high-resolution TEM (HRTEM) image (Fig. 5(d)) presented a typical stacking sequence arising from the nanolaminate MAX phase structure, where the *c* lattice parameter for the $(Cr_{1-x}Mo_x)_2AlC$ coating at 1.326 nm was slightly larger than that at 1.282 nm for the Cr_2AlC phase [17]. The reason for this difference could be reasonably due to the substitution of larger Mo atoms for smaller Cr atoms in the M-site of the MAX phase matrix. Compared with the SEM and TEM data, solid solutions with different Mo concentrations in the Cr_2AlC MAX phase not only favored a dense structure with high-purity MAX phases but also played a crucial role in refining the crystal grain size for the hierarchical structure simultaneously.

Figure 6 presents the detailed microstructural characterization of the solid-solution alloyed coating by the advanced atom-resolved high-angle annular dark-field (HAADF) technique. As expected, the crystal structure and atom arrangements of $(Cr_{1-x}Mo_x)_2AlC$ MAX phase along the $[11\bar{2}0]$ zones were unambiguously identified from the HAADF-STEM images of the skin layer in the coating (Fig. 6(a)). The contrast intensity of HAADF images could be closely related to the atomic number, in which higher atomic numbers are associated with greater contrast intensity [28]. In other words, this distinctly nanolayered structure was mainly composed of alternating stacks with two layers of (Cr,Mo)–C slabs and an interleaved layer of Al atoms, yet the absence of C atoms arose from the rather weak diffraction power in the STEM image. In the enlarged view of the selected region outlined by the red box in Fig. 6(a), much brighter and larger atoms were identified at the M-site Cr position in the Cr_2AlC matrix, as demonstrated by the marked area with yellow arrows and the schematic structure of the nanolayered crystal cells. Most importantly, since Mo atoms have a larger atomic radius and atomic number than Cr atoms do, these distinctive brighter atoms were confidently elucidated as Mo atoms without suspicion. The corresponding EDS mapping results (Figs. 6(c)–6(h)) also revealed the existence of solid-Mo atoms at the Cr site in the

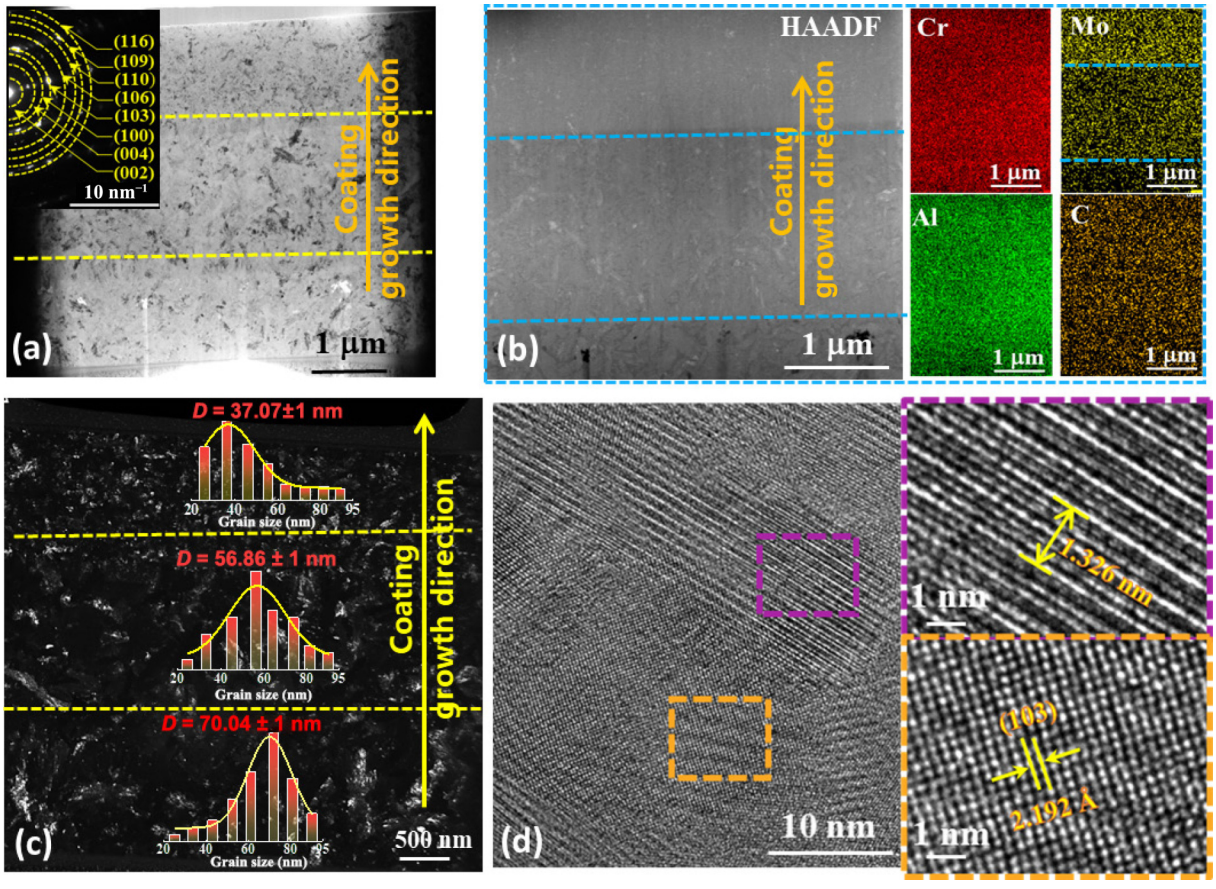

Fig. 5 TEM images of cross section of $(Cr_{1-x}Mo_x)_2AlC$ coating. (a) Bright-field image with corresponding SAED pattern. (b) High-angle annular dark field image with corresponding EDS mappings. (c) Dark-field image with calculated grain size distributions. (d) HRTEM images.

Cr_2AlC phase. As shown in the inserted EDS mapping spectrum (Fig. 6(h)), these nanocrystalline particulates essentially consisted of Cr, Mo, Al, and C, namely, Cr-36.32 at%, Mo-11.62 at%, Al-24.35 at%, and C-27.71 at%. Furthermore, the molar ratio of (Cr+Mo) to Al was close to 2 : 1. In this regard, the partial M-site of Cr in the Cr_2AlC coating was successfully occupied by solid-solution Mo atoms, confirming the facile manipulation of the $(Cr_{1-x}Mo_x)_2AlC$ phase coating. Moreover, increasing the Mo concentration could easily promote the refinement of the grain size toward a hierarchical structure. This unique structure could be an expected strategy to overcome the strength-ductility trade-off for the nanolaminate MAX phase used in the desired application scenarios.

3.2 Mechanical properties of $(Cr_{1-x}Mo_x)_2AlC$ coating

To evaluate the dependence of the mechanical properties on the microstructural evolution in $(Cr_{1-x}Mo_x)_2AlC$ MAX phase coatings, nanoindentation tests were performed for comparative coatings. Figure 7 shows the average hardness (H), elastic modulus (E), H/E, and H^3/E^2 of the three MAX phase coatings assigned to the Cr_2AlC, monolayer $(Cr_{0.8}Mo_{0.2})_2AlC$, and hierarchical $(Cr_{1-x}Mo_x)_2AlC$ samples, respectively. Generally, hardness embodies the capacity to withstand plastic deformation when the indenter is depressed, whereas a high elastic modulus signifies substantial resistance to deformation under a specified load [29]. Moreover, the H/E ratio is frequently employed to qualitatively assess the failure resistance of materials, where a high value indicates the exceptional toughness of the material, particularly in the domain of hard coatings [30–32]. On the other hand, the H^3/E^2 ratio represents the ability of a coating to resist plastic deformation [33]. Compared with the pristine Cr_2AlC coating, both coatings with a Mo solid solution revealed remarkable increases in hardness, elastic modulus, and H/E and H^3/E^2 values. Specifically, the maximum value of H at 16.35 GPa was found in the case of the hierarchical $(Cr_{1-x}Mo_x)_2AlC$ gradient coating, which was approximately 26% greater than that of the Cr_2AlC coating. Furthermore, interestingly, the largest values of H/E at 0.064 and H^3/E^2 at 0.066 were also obtained in the hierarchical sample, which were approximately 12% and 57% greater than those of the pristine Cr_2AlC coating. As expected, a solid solution of Mo in the Cr_2AlC coating effectively enhanced the mechanical properties. Interestingly, unlike the uniform solid-Mo solution coating, tailoring the Mo concentration in the $(Cr_{1-x}Mo_x)_2AlC$ structure enabled easy manipulation of the gradient refinement of the crystal grain size, particularly naming a hierarchical structure toward high hardness-toughness synergy in the MAX phase coating.

Furthermore, we carried out indentation tests with heavy cube-corner tips to reveal the changes in the fracture toughness of the coatings. As shown in the bottom parts of Fig. 7, the surface morphologies concentrated around the indentation center were quite similar for both the Cr_2AlC and $(Cr_{0.8}Mo_{0.2})_2AlC$ coatings, and no distinct variety was visible from the radial cracks, and the crack lengths aligned with the extension tendency. This result suggested the limited enhancement of fracture toughness by only the Mo solid solution for the Cr_2AlC coating; even minor changes from a pristine triangle shape to an obtuse shape were induced from the indentation morphology. In contrast to both pristine and uniform Mo solid solutions at a fixed concentration, however, a direct observation revealed that no cracks surrounded the

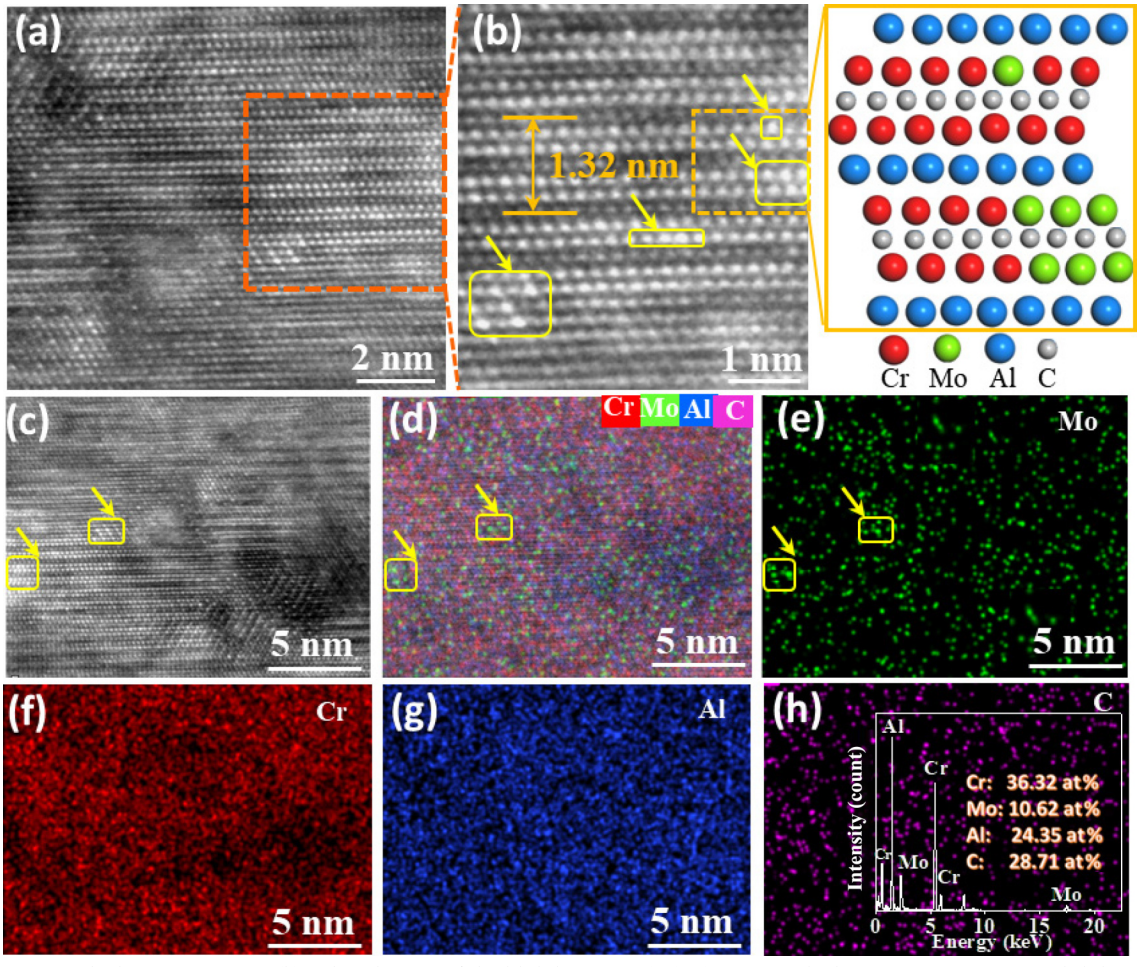

Fig. 6 (a) Atom-resolved HAADF images. (b) Enlarged image of the labeled area in (a). (c–g) Atom-resolved EDS mapping images and deduced elemental concentrations.

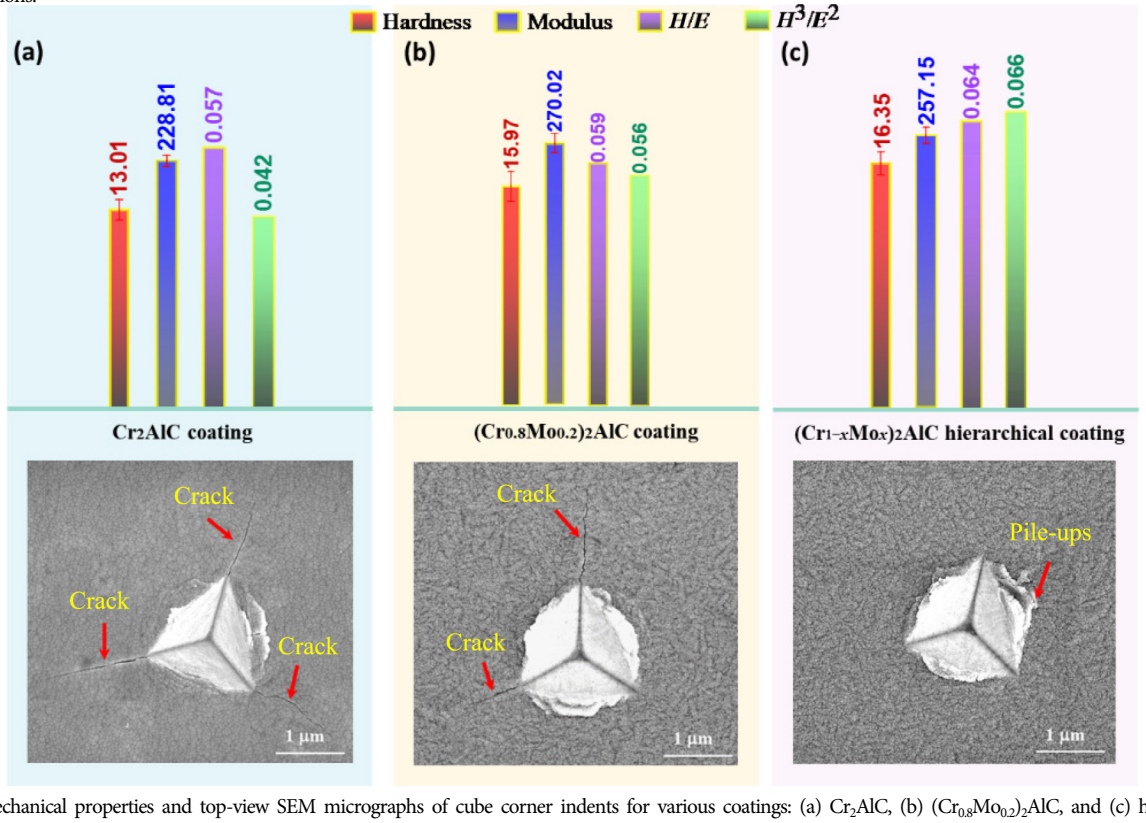

Fig. 7 Mechanical properties and top-view SEM micrographs of cube corner indents for various coatings: (a) Cr_2AlC, (b) $(Cr_{0.8}Mo_{0.2})_2AlC$, and (c) hierarchical $(Cr_{1-x}Mo_x)_2AlC$ samples.

清華大学出版社 Tsinghua University Press | SciOpen

indentation corner or radical edges, accompanied by the appearance of a clear pile-up morphology. These in-depth results revealed a significant increase in fracture toughness in the hierarchical $(Cr_{1-x}Mo_x)_2AlC$ coatings, which is consistent with the above variation in H/E and H^3/E^2 values.

In addition to the experimental results, atomic-scale first-principle calculations were further performed to elucidate the effect of the Mo solid solution on the elastic constant (C_{ij}), which generally plays a crucial role in determining the mechanical properties and structural stability of materials [34]. In the case of the hexagonal Cr_2AlC MAX phase, C_{ij} can be independently represented by five constants, namely, C_{11}, C_{12}, C_{13}, C_{33}, and C_{44}. Figure 8(a) shows the applicable structural models, and the elastic constants were subsequently calculated for $(Cr_{1-x}Mo_x)_2AlC$ with various Mo concentrations, where x was 0.0625, 0.1250, 0.1875, and 0.2500. As shown in Fig. 8(b), all the elastic constants of C_{ij} were positive and satisfied the mechanical stability criteria [35, 36], particularly where $C_{11} > 0$, $C_{11} - C_{12} > 0$, $C_{44} > 0$, and $(C_{11} + C_{12})C_{33} - 2C_{13}^2 > 0$. Here, C_{11} and C_{33} were used to anticipate the stiffness of the material along the [100] and [001] directions, respectively. For all the pristine Cr_2AlC and Mo solid solution samples, greater stiffness along the [100] direction than along the [001] direction was clearly observed, implying that these coatings were more susceptible to deformation along the crystallographic a-axis than along the c-axis. On the other hand, since the elastic constant C_{44} is generally proportional to the hardness of materials [37], the remarkable increase in C_{44} for coatings with a Mo solid solution revealed the expected improvement in the hardness of the Cr_2AlC MAX phase coating via the substitution of Cr with Mo at the M-site.

Figure 8(c) displays the calculated values of the bulk modulus (B), shear modulus (G), and Young's modulus (Y) of the investigated systems. Among the three modulus parameters, both B and G can be responsible for the failure mode of solids, such as brittle or ductile failure. During brittle failure, materials experience sudden fracture, whereas ductile failure involves plastic deformation before eventual fracture. According to Pugh's reports [38], the B/G ratio could be a useful tool for identifying a material as either brittle or ductile. Specifically, when the value of B/G exceeds 1.75, the material is dominated by ductile characteristics; otherwise, brittle failure will be inherently displayed for B/G values less than 1.75. Compared with that of the Cr_2AlC phase, an increasing trend in each modulus was obtained for the $(Cr_{1-x}Mo_x)_2AlC$ solid solution samples (Fig. 8(c)), indicating that the partial substitution of Mo for Cr contributed to the enhanced mechanical performance. In addition, all the Cr_2AlC coatings had B/G values less than 1.75, implying that the Cr_2AlC coatings were predominantly brittle regardless of the Mo solid solution. This was consistent with the intrinsic brittleness typically observed in bulk MAX phases [39,40]. However, in contrast to the B/G value of 1.24 for the pristine Cr_2AlC case, the introduction of a Mo solid-solution into the MAX phase with x values ranging from 0.0625 to 0.2500 led to a remarkable increase in B/G, which ranged from 1.37 to 1.43. Therefore, the increase in B/G reflected the increase in toughness in the $(Cr_{1-x}Mo_x)_2AlC$ systems, which was primarily responsible for solid solution strengthening.

3.3 Strengthening mechanism of $(Cr_{1-x}Mo_x)_2AlC$ coating

Compared with both the pristine Cr_2AlC coating and $(Cr_{0.8}Mo_{0.2})_2AlC$ coating, high hard- yet-tough performance was clearly achieved in the hierarchical $(Cr_{1-x}Mo_x)_2AlC$ coating with a refined grain size gradient. These observations could be attributed to two factors. First, unlike the homogenous structure with a uniform grain size, the gradient refinement of the grain size was promoted by increasing the solid-Mo concentration along the growth direction in the MAX phase matrix. In this case, the

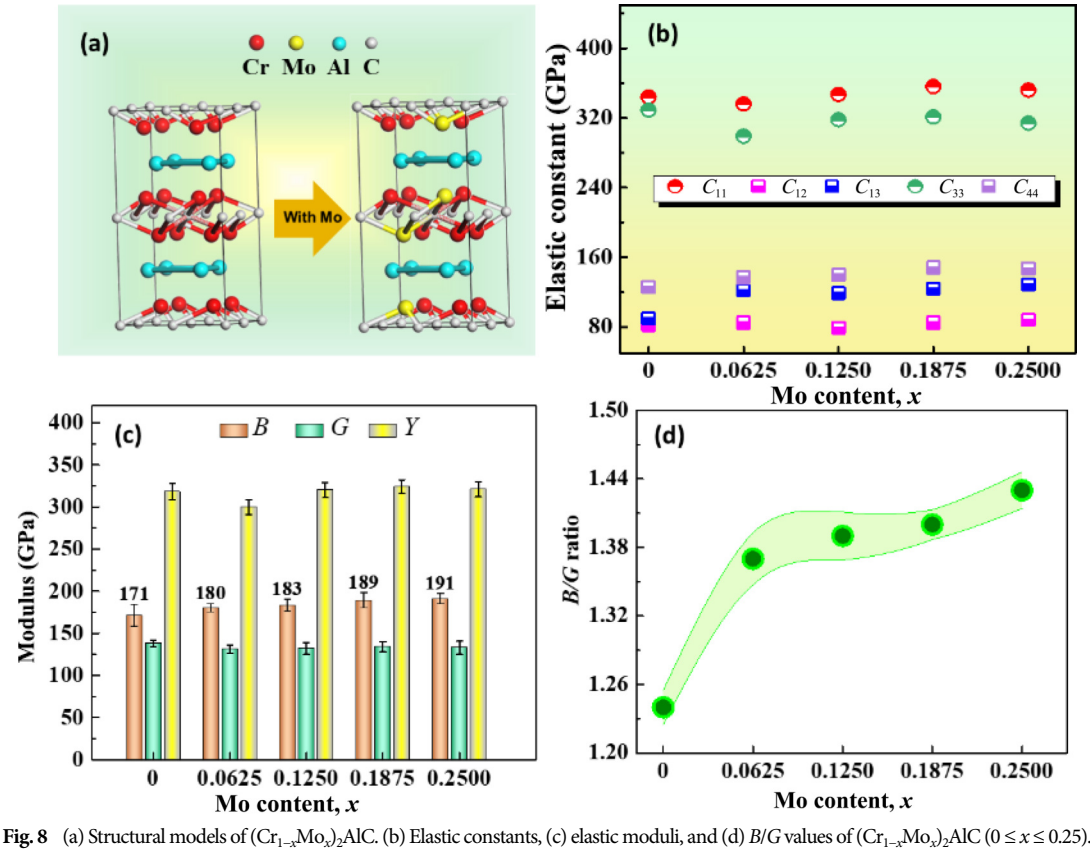

Fig. 8 (a) Structural models of $(Cr_{1-x}Mo_x)_2AlC$. (b) Elastic constants, (c) elastic moduli, and (d) B/G values of $(Cr_{1-x}Mo_x)_2AlC$ ($0 \le x \le 0.25$).

localized stress would be alleviated for a more uniform distribution, which subsequently led to the prevention of strain localization. Moreover, additional strain hardening emerged within gradient layers and in regions where the transition of grain size might occur, ultimately suppressing the propagation path and velocity of cracks [41–44]. This was the key contribution to the extraordinary ductility of materials with hierarchical structures. Second, the hardness increase in the hierarchical $(Cr_{1-x}Mo_x)_2AlC$ coating might be strongly due to the refinement of crystal grain sizes related to various Mo concentrations [45]. Notably, the correlation between hardness and grain size can generally be described by the Hall-Petch relationship [46–49]. Therefore, to thoroughly elucidate the impact of grain size on hardness in the hierarchical $(Cr_{1-x}Mo_x)_2AlC$ coating, the hardness distribution of each layer was analyzed, and the variation in hardness values of each layer, as a function of the inverse of the square root of the grain size, is illustrated in Fig. 9. The fitting result of the data aligned with a single trend line led to the conclusion that the pattern of hardness fluctuation within each layer of the hierarchical $(Cr_{1-x}Mo_x)_2AlC$ coating followed the Hall-Petch relationship as the grain size decreased.

Another benefit for the hardness increases in the hierarchical $(Cr_{1-x}Mo_x)_2AlC$ coating might be the variation in the atomic bonding characteristics. Figure 10 displays the electronic density of states (DOS) and electronic charge density maps for both Cr_2AlC and various $(Cr_{1-x}Mo_x)_2AlC$ systems based on DFT calculations for comparison. The mixed bonding characteristic of Cr_2AlC can be deduced from Fig. 10(a), where the peak at approximately −2.5 eV was mainly composed of Cr 3d and Al 3p orbitals, whereas the peaks at lower energies ranging from −15 to −10 eV and from −7 to −3 eV were assigned to the Cr 3d and C 2p/2s states, respectively. This result indicated the strong hybridization of the Cr 3d and Al 3p orbitals, as well as the Cr 3d and C 2p/2s orbitals, which agreed well with other reports [50,51]. Moreover, on the basis of the energy range of hybridization, the Cr-C bonds presented a greater bonding strength than the Cr-Al bonds did. The electrons occupying the Fermi level are mainly favored by Cr, suggesting that the Cr-Cr metallic bond is responsible for conducting electrons. After the introduction of the Mo atom into the Cr site in the Cr_2AlC structure, all DOSs of the $(Cr_{1-x}Mo_x)_2AlC$ systems exhibited bonding characteristics similar to those of the pristine Cr_2AlC case (Fig. 10(b)). However,

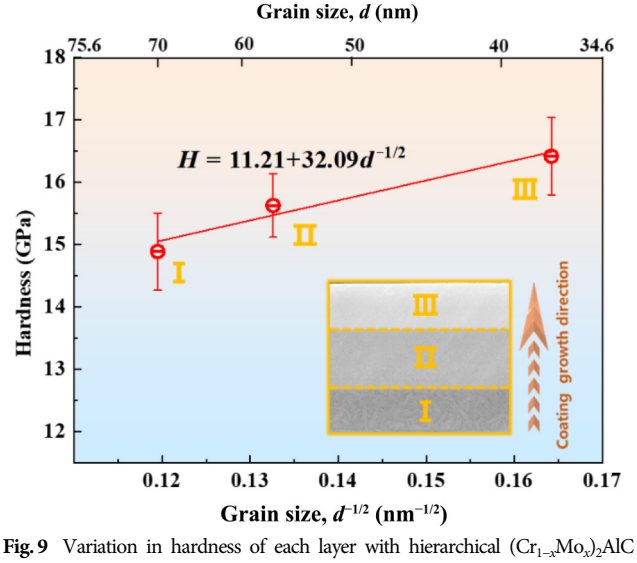

Fig. 9 Variation in hardness of each layer with hierarchical $(Cr_{1-x}Mo_x)_2AlC$ coating as a function of inverse of square root of grain size.

increasing the Mo concentration enabled the hybridized peaks of the Cr-C bonds to shift downward gradually (Fig. 10(c)), confirming the increase in the number of Cr-C covalent bonds, whereas the bonding of Cr-Al did not significantly change with increasing Mo concentration. Typically, the covalent bonds between M and X atoms in MAX phases endow these materials with relatively high elastic moduli and strengths, whereas the weak bonds between M and A atoms allow MAX phase materials to possess a certain degree of fracture toughness. In other words, the increase in the number of Cr-C covalent bonds potentially contributed to the increased hardness of $(Cr_{1-x}Mo_x)_2AlC$ compared with that of Cr_2AlC.

Figure 10(d) further shows the charge density maps for $(Cr_{1-x}Mo_x)_2AlC$ coatings with various Mo concentrations obtained via DFT calculations. The atomic positions were labeled to address the accumulation and depletion of electronic charge. The scale on the right side of the contour plot specifies the intensity of the charge (electron) density, while the red and blue colors indicate high and low electron densities, respectively. Regardless of the Mo solid solution, all the systems exhibited accumulated and overlapped charges in the regions around the Cr-C bonds, which is the covalent bonding characteristic [52,53]. In particular, as the Mo concentration x increased from 0.0625 to 0.2500 in the $(Cr_{1-x}Mo_x)_2AlC$ system, the charges significantly gathered around the Cr–C regions, which evidenced the increased bonding strength around Cr–C from the DOS results. Therefore, the hierarchical $(Cr_{1-x}Mo_x)_2AlC$ coatings had better mechanical properties than did the homogenous Cr_2AlC coating.

For simplicity, Fig. 11 shows the comparative results of hardness and H/E for several Cr_2AlC coatings in this study and other references. The distinct observation was that, different from the fatal limits of hardness toughness reported in previous studies, a higher hardness value of 16.35 GPa together with the largest H/E value of 0.064 were simultaneously achieved by manipulating the hierarchical $(Cr_{1-x}Mo_x)_2AlC$ coating with gradient refined grain sizes. In particular, theoretical calculations revealed that a solid solution of Mo atoms at Cr sites in the Cr_2AlC MAX phase significantly enhances the atomic covalent bonding of Cr–C. The increase in atomic bonding and grain refinement essentially multiplied the hardness of the hierarchical structured $(Cr_{1-x}Mo_x)_2AlC$ coating. More importantly, tailoring the Mo concentration from lower to larger amounts led to a gradient decrease in the crystal grain size from 70.04±1 to 37.07±1 nm along the growth direction. This hierarchically dense structure with a refined grain size increased the toughness without sacrificing the hardness simultaneously. The evidence is that both the hardness and toughness of the hierarchical structured $(Cr_{1-x}Mo_x)_2AlC$ MAX phase coating improved by approximately 26% and 13%, respectively, compared with those of the pristine Cr_2AlC coating, which is also quite beyond the hardness-toughness limits reported in the literature.

4 Conclusions

In summary, $(Cr_{1-x}Mo_x)_2AlC$ MAX phase coatings were successfully fabricated via a multitarget magnetron sputtering system combined with *ex situ* vacuum annealing. Increasing the x value from 0.05 to 0.24 gradually led to an interesting hierarchical structure with refined nanograin sizes from approximately 70.04 to 37.07 nm along the growth direction. Furthermore, the atom-resolved TEM characterization clearly revealed the occupancy of Mo at partial Cr sites and the presence of a gradient variation in the crystal grains. The combination of nanoindentation tests revealed that the hierarchical structure of the $(Cr_{1-x}Mo_x)_2AlC$

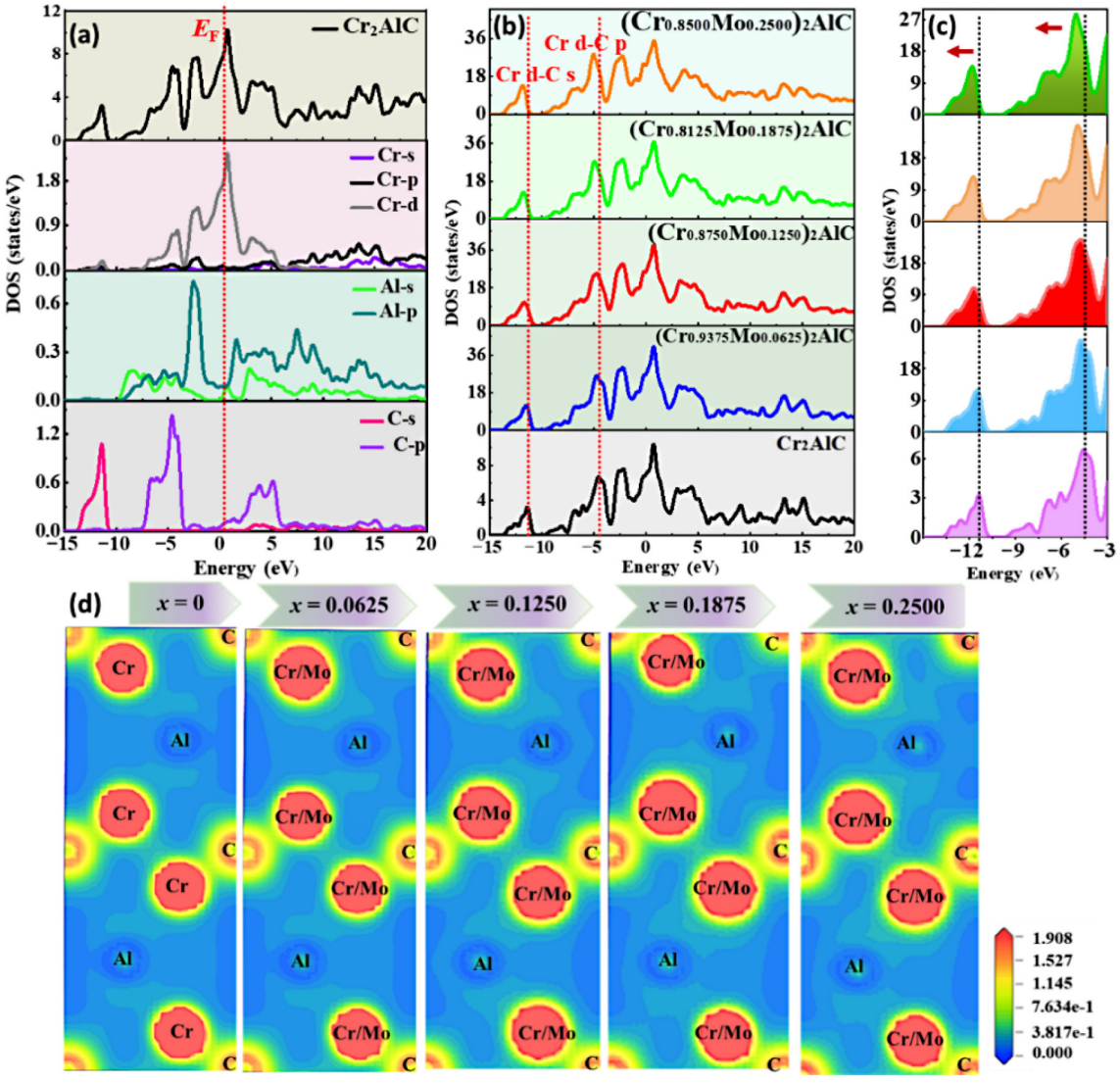

Fig. 10 (a) Total density of states (DOS) and partial density of states of Cr_2AlC. (b) Total density of states (DOS) of $(Cr_{1-x}Mo_x)_2AlC$ ($0 \le x \le 0.25$). (c) Enlarged view of selected region in (b). (d) Electronic charge density maps of corresponding $(Cr_{1-x}Mo_x)_2AlC$ systems.

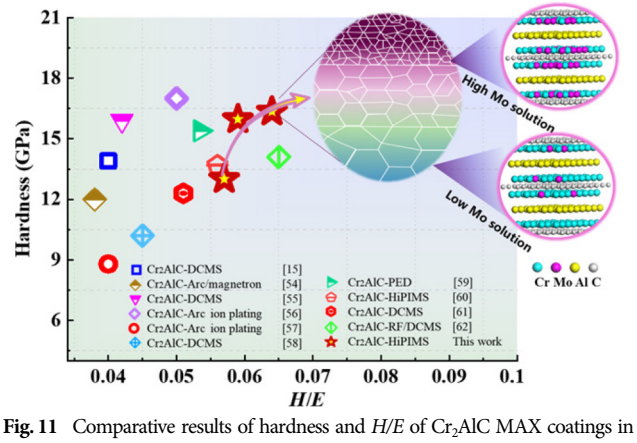

Fig. 11 Comparative results of hardness and H/E of Cr_2AlC MAX coatings in our work and those in Refs. [15,54–62].

coating exhibited synergy between high hardness and toughness. Specifically, the hardness and fracture toughness values of H/E and H^3/E^2 of the hierarchical $(Cr_{1-x}Mo_x)_2AlC$ coating were approximately 26%, 12%, and 57% greater than those of the pristine Cr_2AlC coating, respectively. The reason for this hard-yet-tough observation could be elucidated from two aspects. First, for the hierarchical $(Cr_{1-x}Mo_x)_2AlC$ coating, the increase in hardness might be strongly attributed to the strengthening of the crystallinity with increasing Mo concentration, as well as the increase in Cr–C covalent bonding by the solid solution of Mo atoms at the Cr sites in the Cr_2AlC matrix. Second, the gradient reduction in the nanograin size was the key contributor to the extraordinary toughness of materials with hierarchical structures. Consequently, these results not only identify the solid solution strengthening and gradient hardening synergy for the hardness–toughness trade-off in Cr_2AlC coatings by controlling the Mo solid solution but also suggest a promising strategy to develop advanced MAX phase materials with the required strength–toughness together with other combinations of ceramics and metals.

Acknowledgements

Yan Zhang and Shuowen Zhang contributed equally to this work. This research was supported by the National Science Found for Distinguished Young Scholars of China (No. 52025014), the Zhejiang Provincial Postdoctoral Science Foundation (No. ZJ2023106), the Zhejiang Provincial Natural Science Foundation (No. LQ24E01005), and the Key R&D Program of Ningbo (No. 2024Z096).

Declaration of competing interest

The authors have no competing interests to declare that are relevant to the content of this article.

References

[1] Zhong Y, Liu Y, Jiang QK, *et al.* Improvement of mechanical properties and investigation of strengthening mechanisms on the Ti_3AlC_2 ceramic with nanosized WC addition. *J Adv Ceram* 2024, **13**: 861–876.

[2] Ali MA, Hossain MM, Uddin MM, *et al.* Physical properties of new MAX phase borides M2SB (M = Zr, Hf and Nb) in comparison with conventional MAX phase carbides M2SC (M = Zr, Hf and Nb): Comprehensive insights. *J Mater Res Technol* 2021, **11**: 1000–1018.

[3] Tian ZH, Zhang PG, Sun WW, *et al.* Vegard's law deviating $Ti_2(Sn_xAl_{1-x})C$ solid solution with enhanced properties. *J Adv Ceram* 2023, **12**: 1655–1669.

[4] Barsoum MW. A new class of solids: Thermodynamically stable nanolaminates. *Prog Solid State Ch* 2000, **28**: 201–281.

[5] Xiao H, Zhao S, Liu QY, *et al.* Point defect properties in high entropy MAX phases from first-principles calculations. *Acta Mater* 2023, **248**: 118783.

[6] Fu L, Xia W. MAX phases as nanolaminate materials: Chemical composition, microstructure, synthesis, properties, and applications. *Adv Eng Mater* 2021, **23**: 2001191.

[7] Ching WY, Mo YX, Aryal S, *et al.* Intrinsic mechanical properties of 20 MAX-phase compounds. *J Am Ceram Soc* 2013, **96**: 2292–2297.

[8] Rougab M, Gueddouh A. Exploring elastic anisotropies, mechanical, thermodynamic, optical properties and structural stability of the new possible 312 MAX phases Hf_3GeX_2 (X = C, N and B). *Ab-initio* study. *Comput Theor Chem* 2024, **1233**: 114497.

[9] Yang JS, Ye F, Cheng LF, *et al.* Preparation and properties of Ti_3SiC_2-based corrosion mitigation coatings for SiC_f/SiC PWR accident tolerant fuel cladding. *J Adv Ceram* 2024, **13**: 73–85.

[10] Huang JX, Wan HJ, Li M, *et al.* *In-situ* growth of MAX phase coatings on carbonised wood and their terahertz shielding properties. *J Adv Ceram* 2021, **10**: 1291–1298.

[11] Rakhadilov BK, Maksakova OV, Buitkenov DB, *et al.* Structural-phase and tribo-corrosion properties of composite Ti_3SiC_2/TiC MAX-phase coatings: An experimental approach to strengthening by thermal annealing. *Appl Phys A* 2022, **128**: 145.

[12] Li ZC, Wang ZY, Ma GS, *et al.* High-performance Cr_2AlC MAX phase coatings for ATF application: Interface design and oxidation mechanism. *Corros Commun* 2024, **13**: 27–36.

[13] Lin ZJ, Li MS, Wang JY, *et al.* High-temperature oxidation and hot corrosion of Cr_2AlC. *Acta Mater* 2007, **55**: 6182–6191.

[14] Zakeri-Shahroudi F, Ghasemi B, Abdolahpour H, *et al.* *In situ* coating and hot corrosion behavior of Cr_2AlC MAX phase. *J Mater Eng Perform* 2024, **33**: 5846–5858.

[15] Naveed M, Obrosov A, Zak A, *et al.* Sputtering power effects on growth and mechanical properties of Cr_2AlC MAX phase coatings. *Metals* 2016, **6**: 265.

[16] Qu LS, Bei GP, Stelzer B, *et al.* Synthesis, crystal structure, microstructure and mechanical properties of $(Ti_{1-x}Zr_x)_3SiC_2$ MAX phase solid solutions. *Ceram Int* 2019, **45**: 1400–1408.

[17] Wang ZY, Wang CC, Zhang YP, *et al.* M-site solid solution of vanadium enables the promising mechanical and high-temperature tribological properties of Cr_2AlC coating. *Mater Design* 2022, **222**: 111060.

[18] Su RR, Zhang HL, Ouyang GY, *et al.* Enhanced oxidation resistance of $(Mo_{95}W5)_{85}Ta_{10}(TiZr)_5$ refractory multi-principal element alloy up to 1300 °C. *Acta Mater* 2021, **215**: 117114.

[19] Zhao CC, Xing XL, Guo J, *et al.* Micro-properties of (Nb,M)C carbide (M = V, Mo, W and Cr) and precipitation behavior of (Nb,V)C in carbide reinforced coating. *J Alloys Compd* 2019, **788**: 852–860.

[20] Zhou RN, Wang FM, Xu K, *et al.* Effect of molybdenum addition on oxidation behavior and secondary protection mechanism of FeCrAl coatings. *Mater Charact* 2023, **204**: 113221.

[21] Li XY, Lu L, Li JG, *et al.* Mechanical properties and deformation mechanisms of gradient nanostructured metals and alloys. *Nat Rev Mater* 2020, **5**: 706–723.

[22] Zhang Y, Zhang AF, Li ZC, *et al.* Electrochemical corrosion inhibition of Cr_2AlC MAX phase coatings via Mo solid solution: Comprehensive experimental and simulation study. *J Phys Chem C* 2024, **128**: 3916–3923.

[23] Groden K, Vila FD, Li L, *et al.* First-principles approach to extracting chemical information from X-ray absorption near-edge spectra of Ga-containing materials. *J Phys Chem C* 2021, **125**: 27901–27908.

[24] Segall MD, Lindan PJD, Probert MJ, *et al.* First-principles simulation: Ideas, illustrations and the CASTEP code. *J Phys: Condens Mat* 2002, **14**: 2717–2744.

[25] Perdew J, Burke K, Ernzerhof M. Generalized gradient approximation made simple. *Phys Rev Lett* 1996, **77**: 3865–3868.

[26] Pogrebnjak AD, Ivashchenko VI, Skrynskyy PL, *et al.* Experimental and theoretical studies of the physicochemical and mechanical properties of multi-layered TiN/SiC films: Temperature effects on the nanocomposite structure. *Compos Part B Eng* 2018, **142**: 85–94.

[27] Murnaghan FD. Finite deformations of an elastic solid. *Am J Math* 1937, **59**: 235.

[28] Li ZQ, Wu EX, Chen K, *et al.* Chalcogenide MAX phases $Zr_2Se(B_{1-x}Se_x)$ (x = 0–0.97) and their conduction behaviors. *Acta Mater* 2022, **237**: 118183.

[29] Kim GS, Lee SY, Hahn JH, *et al.* Synthesis of CrN/AlN superlattice coatings using closed-field unbalanced magnetron sputtering process. *Surf Coat Tech* 2003, **171**: 91–95.

[30] Leyland A, Matthews A. On the significance of the H/E ratio in wear control: A nanocomposite coating approach to optimised tribological behaviour. *Wear* 2000, **246**: 1–11.

[31] Musil J, Jaroš M, Čerstvý R, *et al.* Evolution of microstructure and macrostress in sputtered hard Ti(Al,V)N films with increasing energy delivered during their growth by bombarding ions. *J Vac Sci Technol A Vac Surf Films* 2017, **35**: 020601.

[32] Buchinger J, Koutná N, Kirnbauer A, *et al.* Heavy-element-alloying for toughness enhancement of hard nitrides on the example Ti–W–N. *Acta Mater* 2022, **231**: 117897.

[33] Johnson KL. *Contact Mechanics*, Cambridge (UK): Cambridge University Press, 1987.

[34] Ali MA, Qureshi MW. Newly synthesized MAX phase Zr_2SeC: DFT insights into physical properties towards possible applications. *RSC Adv* 2021, **11**: 16892–16905.

[35] Sin'ko GV, Smirnov NA. *Ab initio* calculations of elastic constants and thermodynamic properties of bcc, fcc, and hcp Al crystals under pressure. *J Phys Condens Mat* 2002, **14**: 6989–7005.

[36] Mouhat F, Coudert FX. Necessary and sufficient elastic stability conditions in various crystal systems. *Phys Rev B* 2014, **90**: 224104.

[37] Jhi SH, Ihm J, Louie SG, *et al.* Electronic mechanism of hardness enhancement in transition-metal carbonitrides. *Nature* 1999, **399**: 132–134.

[38] Pugh SF. XCII. Relations between the elastic moduli and the plastic properties of polycrystalline pure metals. *Lond Edinb Dublin Philos Mag J Sci* 1954, **45**: 823–843.

[39] Ali MA, Hossain MM, Uddin MM, *et al.* The rise of 212 MAX phase borides: DFT insights into the physical properties of Ti_2PB_2, Zr_2PbB_2, and Nb_2AB_2 [A = P, S] for thermomechanical applications. *ACS Omega* 2023, **8**: 954–968.

[40] Hadi MA, Roknuzzaman M, Chroneos A, *et al.* Elastic and thermodynamic properties of new $(Zr_{3-x}Ti_x)AlC_2$ MAX-phase solid solutions. *Comp Mater Sci* 2017, **137**: 318–326.

[41] Qin S, Yang MX, Jiang P, *et al.* Designing structures with combined gradients of grain size and precipitation in high entropy alloys for simultaneous improvement of strength and ductility. *Acta Mater* 2022, **230**: 117847.

[42] Fang TH, Tao NR. Martensitic transformation dominated tensile plastic deformation of nanograins in a gradient nanostructured 316L stainless steel. *Acta Mater* 2023, **248**: 118780.

[43] Griesbach C, Bronkhorst CA, Thevamaran R. Crystal plasticity simulations reveal cooperative plasticity mechanisms leading to enhanced strength and toughness in gradient nanostructured metals. *Acta Mater* 2024, **270**: 119835.
[44] Lu K. Making strong nanomaterials ductile with gradients. *Science* 2014, **345**: 1455–1456.
[45] Yuan JH, Zhou SH, Wu HC, *et al.* Ultrahigh strength–ductility of nanocrystalline Cr_2AlC coating under micropillar compression. *Scripta Mater* 2023, **235**: 115594.
[46] Naik SN, Walley SM. The Hall–Petch and inverse Hall–Petch relations and the hardness of nanocrystalline metals. *J Mater Sci* 2020, **55**: 2661–2681.
[47] Bhansali K, Keche AJ, Gogte CL, *et al.* Effect of grain size on Hall–Petch relationship during rolling process of reinforcement bar. *Mater Today Proc* 2020, **26**: 3173–3178.
[48] Hakamada M, Nakamoto Y, Matsumoto H, *et al.* Relationship between hardness and grain size in electrodeposited copper films. *Mater Sci Eng A* 2007, **457**: 120–126.
[49] Pogrebnjak AD. Hard and superhard nanostructured and nanocomposite coatings. Nanomaterials-Based Coatings. In: *Nanomaterials-Based Coatings*. Phuong Nguyen Tri, Sami Rtimi, Claudiane M. Ouellet Plamondon, Eds. Elsevier, 2019: 237–337.
[50] Li N, Mo YX, Ching WY. The bonding, charge distribution, spin ordering, optical, and elastic properties of four MAX phases Cr_2AX (A = Al or Ge, X = C or N): From density functional theory study. 2013, **114**: 183503.
[51] Wang CJ, Zhang WG, Han ZB, *et al.* Behaviors of helium in Cr_2AlC from first principles. *J Am Ceram Soc* 2018, **101**: 5771–5780.
[52] Khatun R, Rahman MA, Hossain KM, *et al.* Physical properties of MAX phase Zr_2PbC under pressure: Investigation via DFT scheme. *Phys B Condens Matter* 2021, **620**: 413258.
[53] Qureshi MW, Ma XX, Tang GZ, *et al.* Theoretical predictive screening of noble-metal-containing M_3AuC_2 (M = Ti, V, and Cr) MAX phases. *Comput Mater Sci* 2022, **202**: 111013.
[54] Yuan JH, Wang ZY, Ma GS, *et al.* MAX phase forming mechanism of M–Al–C (M = Ti, V, Cr) coatings: *in situ* X-ray diffraction and first-principle calculations. *J Mater Sci Technol* 2023, **143**: 140–152.
[55] Obrosov A, Gulyaev R, Zak A, *et al.* Chemical and morphological characterization of magnetron sputtered at different bias voltages Cr–Al–C coatings. *Materials* 2017, **10**: 156.
[56] Liu FJ, Cao HS, Li H, *et al.* Effect of annealing on the microstructure, mechanical and electrochemical properties of CrAlC coatings. *Surf Coat Technol* 2022, **447**: 128800.
[57] Li YM, Zhao GR, Du BN, *et al.* Fabrication of Cr_2AlC coating from a cost-efficient Cr–Al–C target by arc ion plating. *Surf Innov* 2019, **7**: 4–9.
[58] Grieseler R, Hähnlein B, Stubenrauch M, *et al.* Nanostructured plasma etched, magnetron sputtered nanolaminar Cr_2AlC MAX phase thin films. *Appl Surf Sci* 2014, **292**: 997–1001.
[59] Zamulaeva EI, Levashov EA, Sviridova TA, *et al.* Pulsed electrospark deposition of MAX phase Cr_2AlC based coatings on titanium alloy. *Surf Coat Tech* 2013, **235**: 454–460.
[60] Eichner D, Schlieter A, Leyens C, *et al.* Solid particle erosion behavior of nanolaminated Cr_2AlC films. *Wear* 2018, **402**: 187–195.
[61] Li YM, Zhao GR, Qian YH, *et al.* Deposition of phase-pure Cr_2AlC coating by DC magnetron sputtering and post annealing using Cr–Al–C targets with controlled elemental composition but different phase compositions. *J Mater Sci Technol* 2018, **34**: 466–471.
[62] Tang CC, Steinbrück M, Grosse M, *et al.* The effect of annealing temperature on the microstructure and properties of Cr–C–Al coatings on zircaloy-4 for accident-tolerant fuel (ATF) applications. *Coatings* 2022, **12**: 167.